Forward–Backward Indirect Shooting for Low-Thrust Trajectories with Interior Events

Zhong Zhang[(1,2)], Jia Yang[(2)], Dario Izzo[(3)], and Francesco Topputo[(1)]

[(1)]Department of Aerospace Science and Technology, Politecnico di Milano, 20156 Milan, Italy
[(2)]School of Aerospace Engineering, Tsinghua University, Beijing 100084, China
[(3)]Advanced Concepts Team, European Space Research and Technology Centre, European Space Agency, 2201 AZ Noordwijk, The Netherlands

Emails: zhong.zhang@polimi.it

***Abstract* - Physical interior events, such as flybys, asteroid encounters, prescribed waypoints, and collision-avoidance constraints, introduce equality constraints inside optimal-control problems. In the indirect method, these constraints may create a discontinuity in costate. This paper introduces a forward–backward shooting residual that enforces the event optimality conditions without without introducing the costate jump as an explicit shooting unknown, thereby improving local convergence and enabling joint two-arc designs. The contributions are fourfold: (i) a two-sided optimality-residual construction that recovers the costate jump from propagated arcs; (ii) residual derivation for gravity assists, moving asteroid encounters, powered-descent waypoints, and collision-avoidance constraints; (iii) a joint collision-avoidance and return design showing a significant fuel-consumption reduction in our test case; and (iv) a comparison among shooting formulations showing consistently stronger convergence than single and two-forward shooting under the same random initialization.**

I. Introduction

Low-thrust electric propulsion reduces propellant use through high specific impulse [1] and has been demonstrated by Deep Space 1 [2] and Dawn [3]. Its continuous thrust profile, however, turns trajectory design into an infinite-dimensional optimal-control problem rather than a finite impulsive-maneuver search.

Continuous-thrust trajectories are commonly optimized by direct discretization or indirect shooting [4]. Direct methods solve a finite nonlinear program; indirect methods solve a compact state-costate boundary-value problem that can yield accurate solutions. The latter is now-days well suited for learning-assisted design because it is easy to generates and store large trajectory datasets [5, 6, 7, 8].

Physical interior events make indirect shooting harder. Here they are intermediate equality constraints imposed by mission geometry, target bodies, or safety requirements. The four cases in this paper cover gravity assists, moving small-body encounters, powered-descent fixed points, and collision-avoidance constraints, which correspond to velocity maps, moving-target equalities, fixed points, and scalar safety equalities [9, 10, 11, 12, 13, 14, 15, 16, 17, 18].

For such events, Pontryagin Maximum Principle (PMP) conditions involve one-sided costates and, for position constraints, a position-costate jump [19, 20]. Single shooting can enforce these conditions only by sampling an event multiplier, a costate jump, or an equivalent post-event costate [21, 22]; these variables are valid but poorly scaled because endpoint conditions do not determine their magnitude or direction [22, 23].

Classical multi-arc shooting reduces sensitivity by propagating shorter arcs and matching them [24, 25, 26, 27, 28]. At an artificial patch point, state-costate continuity is appropriate; at a physical event, a moving target, flyby map, or event-specific jump condition may replace that continuity. Treating the event as an ordinary patch point would therefore impose the wrong condition or reintroduce event-local unknowns.

The proposed formulation keeps two-sided propagation but replaces patch-point continuity with physical-event optimality. The pre-event arc is propagated forward and the post-event arc backward, so the one-sided states, costates, and Hamiltonians are evaluated after propagation. The residual then enforces the state, velocity-map or continuity, costate, and Hamiltonian conditions, while recovering the position-costate jump from one-sided costates instead of sampling it.

The contributions are fourfold: a two-sided event residual that recovers the position-costate jump from propagated arcs; residual specializations for a gravity-assist map, a moving small-body encounter, a powered-descent waypoint, and a coupled formulation in which the avoidance and return arcs are associated with the same physical event; and a comparison with single- and two-forward shooting methods under the same random initialization scheme.

The numerical experiments support this mechanism. In Cases A–D, the forward–backward residual always improves convergence. In Case D, the joint two-arc formulation also reduces the fixed-phase fuel consumption by about 49% relative to a sequential design. These results indicate that the benefit is not simply due to adding arcs, but to placing the shooting unknowns on boundary quantities that are easier to initialize.

II. Indirect Shooting Formulation with Physical Interior Events

This section introduces the indirect shooting formulation used for physical interior events. A one-dimensional example is first used to show how the costate jump appears and how it can be eliminated from the shooting vector.

A. One-Dimensional Example

Consider a one-dimensional dynamics $\dot{r} = v$, $\dot{v} = u$ with performance index $J = \int_{t_0}^{t_f} \frac{1}{2} u^2 \, dt$. The initial and terminal states are prescribed:

$$r(t_0) = r_0, \quad v(t_0) = v_0, \quad r(t_f) = r_f, \quad v(t_f) = v_f.$$

The Hamiltonian is $\mathcal{H} = \lambda_r v + \lambda_v u + \frac{1}{2}u^2$. Minimization with respect to the control gives

$$\frac{\partial \mathcal{H}}{\partial u} = \lambda_v + u = 0, \quad u^\star = -\lambda_v.$$

The reduced Hamiltonian is therefore $\bar{\mathcal{H}} = \lambda_r v - \frac{1}{2}\lambda_v^2$. The state–costate equations are

$$\dot{r} = v, \qquad \dot{v} = -\lambda_v, \qquad \dot{\lambda}_r = 0, \qquad \dot{\lambda}_v = -\lambda_r.$$

Now impose a physical interior event. The trajectory must pass through a prescribed moving point $r_c(\tau)$ at a free interior time τ:

$$g(r(\tau), \tau) = r(\tau) - r_c(\tau) = 0, \qquad \tau \in (t_0, t_f).$$

Introduce the event multiplier ξ. Based on PMP conditions, the costate conditions at the event are

$$\begin{bmatrix} \lambda_r^- - \lambda_r^+ \\ \lambda_v^- - \lambda_v^+ \end{bmatrix} = \begin{bmatrix} \partial g/\partial r \\ \partial g/\partial v \end{bmatrix} \xi = \begin{bmatrix} 1 \\ 0 \end{bmatrix} \xi.$$

Thus,

$$\lambda_r^- - \lambda_r^+ = \xi, \qquad \lambda_v^- - \lambda_v^+ = 0. \tag{1}$$

Here, superscripts $-$ and $+$ denote one-sided limits immediately before and after the event.

Since the event time is free, the Hamiltonian jump condition is

$$\bar{\mathcal{H}}^- - \bar{\mathcal{H}}^+ + \xi \frac{\partial g}{\partial \tau} = \bar{\mathcal{H}}^- - \bar{\mathcal{H}}^+ - \xi \, \dot{r}_c(\tau) = 0. \tag{2}$$

Using Eq. (1), the multiplier in (3) can be eliminated as:

$$\bar{\mathcal{H}}^- - \bar{\mathcal{H}}^+ - (\lambda_r^- - \lambda_r^+)\dot{r}_c(\tau) = 0. \tag{3}$$

B. Different Shooting Formulations for 1-D Example

The three shooting formulations enforce the same event optimality conditions. They differ only in how the one-sided event quantities are generated.

Single shooting. Single shooting propagates the trajectory forward from t_0. At the event, the pre-event costate λ_r^- is available from propagation, but the post-event costate λ_r^+ is not determined by continuity because λ_r may jump. Therefore, the jump must be introduced explicitly:

$$\Delta\lambda_r = \lambda_r^- - \lambda_r^+.$$

A single-shooting vector for this example is

$$\boldsymbol{z}_{\mathrm{s}} = \begin{bmatrix} \lambda_r(t_0) & \lambda_v(t_0) & \Delta\lambda_r & \tau \end{bmatrix}^{\mathsf{T}}.$$

After the event, propagation continues with

$$\lambda_r^+ = \lambda_r^- - \Delta\lambda_r, \qquad \lambda_v^+ = \lambda_v^-.$$

The corresponding residual is

$$\boldsymbol{R}_{\mathrm{s}} = \begin{bmatrix} r^-(\tau) - r_c(\tau) \\ \bar{\mathcal{H}}^- - \bar{\mathcal{H}}^+ - \Delta\lambda_r \, \dot{r}_c(\tau) \\ r(t_f) - r_f \\ v(t_f) - v_f \end{bmatrix} = \boldsymbol{0}.$$

Thus, single shooting must guess the costate jump before the post-event arc can be propagated.

Multiple Forward Shooting. Multiple shooting separates the pre-event and post-event arcs, and both arcs are propagated forward in time. The post-event arc needs its own initial augmented state, so the one-sided post-event quantities are included in the shooting vector:

$$\boldsymbol{z}_{\mathrm{m}} = \begin{bmatrix} \lambda_r(t_0) & \lambda_v(t_0) & r^+ & v^+ & \lambda_r^+ & \lambda_v^+ & \tau \end{bmatrix}^{\mathsf{T}}.$$

The residual is

$$\boldsymbol{R}_{\mathrm{m}} = \begin{bmatrix} r^- - r_c(\tau) \\ r^+ - r_c(\tau) \\ v^- - v^+ \\ \lambda_v^- - \lambda_v^+ \\ \bar{\mathcal{H}}^- - \bar{\mathcal{H}}^+ - (\lambda_r^- - \lambda_r^+)\dot{r}_c(\tau) \\ r(t_f) - r_f \\ v(t_f) - v_f \end{bmatrix} = \boldsymbol{0}.$$

This formulation does not name the jump as a separate unknown, but it still requires the post-event augmented state to be guessed.

Forward–backward shooting. Forward–backward shooting propagates the two arcs toward the event from opposite directions. The pre-event arc is integrated forward from t_0 to τ, while the post-event arc is integrated backward from t_f to τ. Since the terminal state is prescribed, only the terminal costates are added as post-event unknowns:

$$\boldsymbol{z}_{\text{fb}} = \begin{bmatrix} \lambda_r(t_0) & \lambda_v(t_0) & \lambda_r(t_f) & \lambda_v(t_f) & \tau \end{bmatrix}^\mathsf{T}.$$

Forward propagation gives $r^-, v^-, \lambda_r^-, \lambda_v^-$, and backward propagation gives $r^+, v^+, \lambda_r^+, \lambda_v^+$. The residual is assembled directly as

$$\boldsymbol{R}_{\text{fb}} = \begin{bmatrix} r^- - r_c(\tau) \\ r^+ - r_c(\tau) \\ v^- - v^+ \\ \lambda_v^- - \lambda_v^+ \\ \bar{\mathcal{H}}^- - \bar{\mathcal{H}}^+ - (\lambda_r^- - \lambda_r^+)\dot{r}_c(\tau) \end{bmatrix} = \mathbf{0}.$$

Therefore, the forward–backward formulation does not remove the costate jump. Instead, it avoids guessing the jump before propagation.

C. General Formulation

The preceding derivation is now extended to a general state vector. Let $\boldsymbol{x} \in \mathbb{R}^{n_x}$, $\boldsymbol{u} \in \mathcal{U} \subset \mathbb{R}^{n_u}$, $\boldsymbol{p}$ denote the state, control, and fixed model parameters. The dynamics and objective function are

$$\dot{\boldsymbol{x}} = \boldsymbol{f}(\boldsymbol{x}, \boldsymbol{u}, t; \boldsymbol{p}),$$

$$J = \Phi(\boldsymbol{x}(t_f), t_f) + \int_{t_0}^{t_f} L(\boldsymbol{x}, \boldsymbol{u}, t)\, dt.$$

The Hamiltonian is

$$\mathcal{H}(\boldsymbol{x}, \boldsymbol{\lambda}, \boldsymbol{u}, t) = \boldsymbol{\lambda}^\mathsf{T} \boldsymbol{f}(\boldsymbol{x}, \boldsymbol{u}, t; \boldsymbol{p}) + L(\boldsymbol{x}, \boldsymbol{u}, t).$$

The optimal control satisfies

$$\boldsymbol{u}^\star = \arg\min_{\boldsymbol{u} \in \mathcal{U}} \mathcal{H}(\boldsymbol{x}, \boldsymbol{\lambda}, \boldsymbol{u}, t),$$

and the reduced Hamiltonian is

$$\bar{\mathcal{H}}(\boldsymbol{x}, \boldsymbol{\lambda}, t) = \mathcal{H}(\boldsymbol{x}, \boldsymbol{\lambda}, \boldsymbol{u}^\star, t).$$

The state–costate equations are

$$\dot{\boldsymbol{x}} = \frac{\partial \bar{\mathcal{H}}}{\partial \boldsymbol{\lambda}}, \qquad \dot{\boldsymbol{\lambda}} = -\frac{\partial \bar{\mathcal{H}}}{\partial \boldsymbol{x}}.$$

Indirect shooting thereby solves $\boldsymbol{R}(\boldsymbol{z}) = \mathbf{0}$, where $\boldsymbol{z}$ contains the shooting unknowns and $\boldsymbol{R}$ collects residuals.

Consider a physical interior event at time τ. The one-sided quantities are

$$\boldsymbol{x}^- = \boldsymbol{x}(\tau^-), \qquad \boldsymbol{\lambda}^- = \boldsymbol{\lambda}(\tau^-),$$

$$\boldsymbol{x}^+ = \boldsymbol{x}(\tau^+), \qquad \boldsymbol{\lambda}^+ = \boldsymbol{\lambda}(\tau^+).$$

The corresponding reduced Hamiltonians are

$$\bar{\mathcal{H}}^- = \bar{\mathcal{H}}(\boldsymbol{x}^-, \boldsymbol{\lambda}^-, \tau), \qquad \bar{\mathcal{H}}^+ = \bar{\mathcal{H}}(\boldsymbol{x}^+, \boldsymbol{\lambda}^+, \tau).$$

The general event constraint is then written in a two-sided form

$$\boldsymbol{h}\big(\boldsymbol{x}^-, \boldsymbol{x}^+, \tau, \boldsymbol{q}\big) = \mathbf{0}, \qquad \boldsymbol{h} \in \mathbb{R}^{n_h},$$

where $\boldsymbol{q}$ denotes optional event-local parameters.

Based on PMP conditions, introduce the event multiplier $\boldsymbol{\xi} \in \mathbb{R}^{n_h}$. With the sign convention used here, the event costate conditions are

$$\boldsymbol{\lambda}^- = \left(\frac{\partial \boldsymbol{h}}{\partial \boldsymbol{x}^-}\right)^\mathsf{T} \boldsymbol{\xi}, \qquad \boldsymbol{\lambda}^+ = -\left(\frac{\partial \boldsymbol{h}}{\partial \boldsymbol{x}^+}\right)^\mathsf{T} \boldsymbol{\xi}. \tag{4}$$

These equations determine which costate components are continuous and which components may jump.

If the event-local parameters are free, their stationarity condition is

$$\left(\frac{\partial \boldsymbol{h}}{\partial \boldsymbol{q}}\right)^\mathsf{T} \boldsymbol{\xi} = \mathbf{0}. \tag{5}$$

If the event time is free, the Hamiltonian jump condition is

$$\bar{\mathcal{H}}^- - \bar{\mathcal{H}}^+ + \boldsymbol{\xi}^\mathsf{T} \frac{\partial \boldsymbol{h}}{\partial \tau} = 0. \tag{6}$$

In practice, the event multiplier does not need to be introduced as a global shooting unknown. Define

$$\boldsymbol{A} = \begin{bmatrix} \dfrac{\partial \boldsymbol{h}}{\partial \boldsymbol{x}^-} & -\dfrac{\partial \boldsymbol{h}}{\partial \boldsymbol{x}^+} & \dfrac{\partial \boldsymbol{h}}{\partial \boldsymbol{q}} & \dfrac{\partial \boldsymbol{h}}{\partial \tau} \end{bmatrix}, \boldsymbol{b} = \begin{bmatrix} \boldsymbol{\lambda}^- \\ \boldsymbol{\lambda}^+ \\ \mathbf{0} \\ \bar{\mathcal{H}}^+ - \bar{\mathcal{H}}^- \end{bmatrix}.$$

Equations (4), (5) and (6) can be written compactly as

$$\boldsymbol{b} = \boldsymbol{A}^\mathsf{T} \boldsymbol{\xi}. \tag{7}$$

Therefore, a multiplier exists if and only if $\boldsymbol{b}$ belongs to the column space of $\boldsymbol{A}^\mathsf{T}$.

Let $\boldsymbol{N}$ be a basis for the null space of $\boldsymbol{A}$: $\boldsymbol{A}\boldsymbol{N} = \mathbf{0}$.

Then Eq. (7) is equivalent to

$$\boldsymbol{N}^\mathsf{T} \boldsymbol{b} = \mathbf{0}.$$

Thus, the multiplier is eliminated algebraically.

The multiplier-free event residual can be written as

$$\boldsymbol{R}_{\mathrm{evt}} = \begin{bmatrix} \boldsymbol{h}(\boldsymbol{x}^-, \boldsymbol{x}^+, \tau, \boldsymbol{q}) \\ \boldsymbol{N}^\mathsf{T} \boldsymbol{b} \end{bmatrix} = \boldsymbol{0}.$$

The first block enforces the physical event equations. The second block combines the costate matching conditions, the event-parameter stationarity conditions, and the free-event-time Hamiltonian condition after elimination of the local multiplier.

The above null-space projection provides a compact general formulation for eliminating the multiplier $\boldsymbol{\xi}$. For events with simple structure, however, the same conditions can often be written directly. For example, as in the one-dimensional example we did, if only the position constraint generates a costate discontinuity, the corresponding multiplier can be obtained implicitly through the event Jacobian relation

$$\boldsymbol{\lambda}_r^- - \boldsymbol{\lambda}_r^+ = \boldsymbol{G}_r^\mathsf{T} \boldsymbol{\xi},$$

where $\boldsymbol{G}_r$ denotes the Jacobian of the event constraint with respect to the position variables. The remaining costate components can then be matched directly, while any free event-parameter or free-event-time conditions are evaluated using the recovered one-sided costates.

III. Case A: Dawn Gravity Assist

The first case tests the most restrictive event map considered here: a Dawn Earth–Mars–Vesta gravity assist with an instantaneous velocity change. At the free Mars encounter epoch τ, the spacecraft position is constrained to Mars, the incoming velocity is mapped to the outgoing velocity, and the velocity-costate relation depends on the flyby-map Jacobian. The case therefore tests whether the backward arc can supply the post-Mars costate information required by flyby stationarity. The mission geometry follows published Dawn data and JPL Horizons ephemerides [29, 30]; the archived setup fixes the corresponding epochs, propulsion level, encounter epoch, and reference final mass.

A. Dynamics and Smoothed Throttle Law

The equations are written in Sun two-body nondimensional units with $L_* = 1$ AU. In this subsection, $T_{\max}$ and $I_{\mathrm{sp}} g_0$ denote the scaled propulsion quantities:

$$\dot{\boldsymbol{r}} = \boldsymbol{v}, \qquad \dot{\boldsymbol{v}} = -\frac{\boldsymbol{r}}{r^3} + \frac{T_{\max}}{m} u \boldsymbol{\alpha}, \qquad \dot{m} = -\frac{T_{\max}}{I_{\mathrm{sp}} g_0} u.$$

The smoothed Hamiltonian [31] is

$$\mathcal{H} = \boldsymbol{\lambda}_r^\mathsf{T} \boldsymbol{v} + \boldsymbol{\lambda}_v^\mathsf{T} \left(-\frac{\boldsymbol{r}}{r^3} + \frac{T_{\max}}{m} u \boldsymbol{\alpha} \right) - \lambda_m \frac{T_{\max}}{I_{\mathrm{sp}} g_0} u + \frac{T_{\max}}{I_{\mathrm{sp}} g_0} \left[u - \varepsilon \log(u(1-u)) \right].$$

The optimal thrust direction and throttle are

$$\boldsymbol{\alpha}^\star = -\frac{\boldsymbol{\lambda}_v}{\|\boldsymbol{\lambda}_v\|}, u^\star = \frac{2\varepsilon}{\rho + 2\varepsilon + \sqrt{\rho^2 + 4\varepsilon^2}},$$

and switching function is

$$\rho = 1 - \frac{I_{\mathrm{sp}} g_0 \, \|\boldsymbol{\lambda}_v\|}{m} - \lambda_m.$$

B. Mars Flyby Conditions

The Mars gravity assist uses a two-parameter instantaneous velocity map:

$$\boldsymbol{v}^+ = \Phi(\boldsymbol{v}^-, \boldsymbol{v}_M, \rho_p, \beta), \qquad R_p = R_M, \quad \mu_p = \mu_M.$$

At the event, $\boldsymbol{v}_M = \boldsymbol{v}_M(\tau)$ and $\boldsymbol{a}_M = \dot{\boldsymbol{v}}_M(\tau)$. The Jacobian blocks $\boldsymbol{A} = \partial\Phi/\partial\boldsymbol{v}^-$, $\boldsymbol{B} = \partial\Phi/\partial\boldsymbol{v}_M$, and $\boldsymbol{C} = \partial\Phi/\partial(\rho_p, \beta)$ are evaluated at $(\boldsymbol{v}^-, \boldsymbol{v}_M, \rho_p, \beta)$; the term $\boldsymbol{B}\boldsymbol{a}_M$ accounts for the explicit epoch dependence of the Mars velocity. The interface conditions are

$$\boldsymbol{\lambda}_v^- = \boldsymbol{A}^\mathsf{T} \boldsymbol{\lambda}_v^+, \qquad \lambda_m^- = \lambda_m^+, \qquad \boldsymbol{C}^\mathsf{T} \boldsymbol{\lambda}_v^+ = \boldsymbol{0},$$

and the free-epoch condition is

$$\mathcal{H}^- - \mathcal{H}^+ + (\boldsymbol{\lambda}_r^- - \boldsymbol{\lambda}_r^+)^\mathsf{T} \boldsymbol{v}_M + (\boldsymbol{\lambda}_v^+)^\mathsf{T} \boldsymbol{B} \boldsymbol{a}_M = 0.$$

C. Forward–Backward Residual

The terminal Vesta position and velocity are fixed, final mass is free, and $\lambda_m(t_f) = 0$. The forward–backward shooting vector is $\boldsymbol{z}_{\mathrm{fb}}^{(1)} = (\boldsymbol{\lambda}_{r0}, \boldsymbol{\lambda}_{v0}, \lambda_{m0}, m_f, \boldsymbol{\lambda}_{rf}, \boldsymbol{\lambda}_{vf}, \tau, \rho_p, \beta)$, with 17 unknowns. The residual is

$$\boldsymbol{R}_{\mathrm{fb}}^{(1)} = \begin{bmatrix} \boldsymbol{r}^- - \boldsymbol{r}_M \\ \boldsymbol{r}^+ - \boldsymbol{r}_M \\ \Phi(\boldsymbol{v}^-, \boldsymbol{v}_M, \rho_p, \beta) - \boldsymbol{v}^+ \\ m^- - m^+ \\ \boldsymbol{\lambda}_v^- - \boldsymbol{A}^\mathsf{T} \boldsymbol{\lambda}_v^+ \\ \lambda_m^- - \lambda_m^+ \\ \boldsymbol{C}^\mathsf{T} \boldsymbol{\lambda}_v^+ \\ \mathcal{H}^- - \mathcal{H}^+ + (\boldsymbol{\lambda}_r^- - \boldsymbol{\lambda}_r^+)^\mathsf{T} \boldsymbol{v}_M \\ + (\boldsymbol{\lambda}_v^+)^\mathsf{T} \boldsymbol{B} \boldsymbol{a}_M \end{bmatrix}_{t=\tau}.$$

The residual separates the flyby map from the jump recovery. The backward arc from Vesta supplies $\boldsymbol{\lambda}_v^+$, so the stationarity condition $\boldsymbol{C}^\mathsf{T} \boldsymbol{\lambda}_v^+ = \boldsymbol{0}$ is evaluated from terminal-boundary data rather than from a guessed post-flyby costate. The position-costate jump still enters the Hamiltonian row through $\boldsymbol{\lambda}_r^- - \boldsymbol{\lambda}_r^+$, but it is computed after the two arcs have been propagated.

Figure 1 shows the resulting reference trajectory, throttle history, and one-sided costate norms.

IV. Case B: Solar-Sail Asteroid Encounter

The second case keeps the moving-target nature of an interior event but removes the velocity discontinuity. In a GTOC13-inspired solar-sail transfer, the spacecraft leaves a Vulcan flyby, meets Yandi at the free interior time τ, and arrives at Hoth at the free final time t_f. Both arcs pass through the moving asteroid, while velocity and velocity costate remain continuous, isolating the position-costate jump. The body ephemerides and solar-sail setting follow the GTOC13 problem page [32]; the archived setup fixes the timing, sailcraft, and departure-flyby parameters.

A. Dynamics and Control

The solar-sail state is $\boldsymbol{x} = [\boldsymbol{r}^\mathsf{T}, \boldsymbol{v}^\mathsf{T}]^\mathsf{T}$. In the nondimensional Altaira units used for this example,

$$\dot{\boldsymbol{r}} = \boldsymbol{v}, \qquad \dot{\boldsymbol{v}} = -\frac{\boldsymbol{r}}{r^3} - k(r)(\boldsymbol{n}^\mathsf{T}\boldsymbol{u}_r)^2\boldsymbol{n},$$

where $\boldsymbol{u}_r = -\boldsymbol{r}/r$, $k(r)$ is the sail acceleration coefficient, and $\boldsymbol{n}$ is the sail normal. The corresponding time-optimal Hamiltonian is

$$\mathcal{H} = \boldsymbol{\lambda}_r^\mathsf{T}\boldsymbol{v} + \boldsymbol{\lambda}_v^\mathsf{T}\dot{\boldsymbol{v}} + 1.$$

The closed-loop sail law is written using

$$a_r = \boldsymbol{\lambda}_v^\mathsf{T}\boldsymbol{u}_r, \qquad a_T = \|\boldsymbol{\lambda}_v - a_r\boldsymbol{u}_r\|.$$

With a small regularization δ_s,

$$\tan\alpha_s = \frac{\sqrt{9a_r^2 + 8a_T^2 + \delta_s^2} - 3a_r}{4\sqrt{a_T^2 + \delta_s^2}},$$

$$\boldsymbol{n}^\star = \frac{\cos\alpha_s\,\boldsymbol{u}_r + \sin\alpha_s\,(\boldsymbol{\lambda}_v - a_r\boldsymbol{u}_r)\,/\sqrt{a_T^2+\delta_s^2}}{\left\|\cos\alpha_s\,\boldsymbol{u}_r + \sin\alpha_s\,(\boldsymbol{\lambda}_v - a_r\boldsymbol{u}_r)\,/\sqrt{a_T^2+\delta_s^2}\right\|}.$$

The costate dynamics are obtained from $\dot{\boldsymbol{\lambda}} = -\mathcal{H}_{\boldsymbol{x}}$.

B. Initial Flyby Map

The departure velocity after the Vulcan flyby is generated by the same two-parameter gravity-assist map used in Case A, with the flyby body set to the departure planet:

$$\boldsymbol{v}_0^+ = \Phi(\boldsymbol{v}_0^-, \boldsymbol{v}_P, \rho_p, \beta), \qquad R_p = R_P, \quad \mu_p = \mu_P.$$

The corresponding ρ_p and β derivatives are evaluated at $(\boldsymbol{v}_0^-, \boldsymbol{v}_P, \rho_p, \beta)$. This Vulcan flyby defines the departure boundary condition rather than the physical interior event tested by this benchmark. Its local stationarity conditions are

$$\boldsymbol{\lambda}_{v0}^\mathsf{T}\Phi_{\rho_p} = 0, \qquad \boldsymbol{\lambda}_{v0}^\mathsf{T}\Phi_{\beta} = 0.$$

C. Forward–Backward Residual

The post-event arc is initialized at Hoth with $\boldsymbol{r}(t_f) = \boldsymbol{r}_H(t_f)$, free terminal velocity $\boldsymbol{v}_f$, unknown $\boldsymbol{\lambda}_{rf}$, and $\boldsymbol{\lambda}_{vf} = \boldsymbol{0}$. The forward–backward shooting vector is

$$\boldsymbol{z}_{\text{fb}}^{(2)} = \begin{bmatrix}\boldsymbol{\lambda}_{r0}^\mathsf{T} & \boldsymbol{\lambda}_{v0}^\mathsf{T} & t_f & \rho_p & \beta & \boldsymbol{\lambda}_{rf}^\mathsf{T} & \boldsymbol{v}_f^\mathsf{T} & \tau\end{bmatrix}^\mathsf{T},$$

with 16 unknowns. The 16 residual equations are

$$\boldsymbol{R}_{\text{fb}}^{(2)} = \begin{bmatrix} \boldsymbol{r}^-(\tau) - \boldsymbol{r}_Y(\tau) \\ \boldsymbol{r}^+(\tau) - \boldsymbol{r}_Y(\tau) \\ \boldsymbol{v}^-(\tau) - \boldsymbol{v}^+(\tau) \\ \boldsymbol{\lambda}_v^-(\tau) - \boldsymbol{\lambda}_v^+(\tau) \\ \boldsymbol{\lambda}_{v0}^\mathsf{T}\Phi_{\rho_p} \\ \boldsymbol{\lambda}_{v0}^\mathsf{T}\Phi_{\beta} \\ \mathcal{H}(t_f) - \boldsymbol{\lambda}_{rf}^\mathsf{T}\boldsymbol{v}_H(t_f) \\ \mathcal{H}^-(\tau) - \mathcal{H}^+(\tau) + (\boldsymbol{\lambda}_r^- - \boldsymbol{\lambda}_r^+)^\mathsf{T}\boldsymbol{v}_Y(\tau) \end{bmatrix}.$$

The first two residual blocks place both arcs on Yandi at the same epoch. The next two blocks enforce continuity of the velocity and velocity costate, which do not jump for this encounter model. The last row is the free-interior-time Hamiltonian condition for the moving-target event equality. A single shooting formulation must sample the Yandi position-costate jump before propagation; the forward–backward residual obtains it from the propagated one-sided position costates.

The corresponding reference transfer and recovered event behavior are shown in Fig. 2.

V. Case C: Lunar Landing with a Fixed Point

The third case isolates a fixed point at a prescribed time in a fuel-optimal powered descent. The position constraint still creates a position-costate jump, but the fixed event time removes the interior Hamiltonian row. This case tests whether avoiding an explicit jump guess remains useful when τ is known. Powered-descent guidance provides a familiar constrained landing setting for this test [14, 15]; the archived normalized setup fixes the event point, final time, final mass, and reference costate jump.

A. Normalized Dynamics

The landing case is normalized by length, lunar-gravity, and mass scales; the derived velocity and time scales are used throughout this subsection. The state and costate are

$$\boldsymbol{y} = \begin{bmatrix}\boldsymbol{r}^\mathsf{T} & \boldsymbol{v}^\mathsf{T} & m & \boldsymbol{\lambda}_r^\mathsf{T} & \boldsymbol{\lambda}_v^\mathsf{T} & \lambda_m\end{bmatrix}^\mathsf{T}.$$

The closed-loop equations are

$$\dot{\boldsymbol{r}} = \boldsymbol{v}, \qquad \dot{\boldsymbol{v}} = \frac{T}{m}\hat{\boldsymbol{e}}_T - \frac{\boldsymbol{r}}{r^3}, \qquad \dot{m} = -\frac{T}{v_{\text{ex}}},$$

$$\dot{\boldsymbol{\lambda}}_r = -3\frac{(\boldsymbol{\lambda}_v^\mathsf{T}\boldsymbol{r})\boldsymbol{r}}{r^5} + \frac{\boldsymbol{\lambda}_v}{r^3}, \qquad \dot{\boldsymbol{\lambda}}_v = -\boldsymbol{\lambda}_r,$$

$$\dot{\lambda}_m = \frac{T\,\|\boldsymbol{\lambda}_v\|}{m^2}.$$

The thrust direction and bang-bang thrust level are

$$\hat{\boldsymbol{e}}_T^\star = \frac{\boldsymbol{\lambda}_v}{\|\boldsymbol{\lambda}_v\|}, \qquad S = \frac{\|\boldsymbol{\lambda}_v\|}{m} - \frac{1+\lambda_m}{v_\mathrm{ex}},$$

$$T^\star = \begin{cases} T_\mathrm{max}, & S \geq 0, \\ T_\mathrm{min}, & S < 0. \end{cases}$$

The free-final-time condition used by the benchmark is

$$\psi_f = \boldsymbol{\lambda}_r^\mathsf{T}\boldsymbol{v} - \boldsymbol{\lambda}_v^\mathsf{T}\frac{\boldsymbol{r}}{r^3} + \frac{T\,\|\boldsymbol{\lambda}_v\|}{m} - 1 = 0.$$

B. Interior Event Constraint

The only physical interior event is the fixed position waypoint at the prescribed time τ.

The interior position condition is

$$\boldsymbol{r}(\tau) - \boldsymbol{r}_i = \boldsymbol{0}.$$

Velocity, mass, $\boldsymbol{\lambda}_v$, and λ_m are continuous. The position-costate jump is

$$\Delta\boldsymbol{\lambda}_{r,\tau} = \boldsymbol{\lambda}_r(\tau^-) - \boldsymbol{\lambda}_r(\tau^+),$$

but this jump is recovered from the propagated arcs rather than guessed as a forward–backward shooting variable.

C. Forward–Backward Residual

The forward–backward unknown vector is

$$\boldsymbol{z}_\mathrm{fb}^{(3)} = \begin{bmatrix} \boldsymbol{\lambda}_{r0}^\mathsf{T} & \boldsymbol{\lambda}_{v0}^\mathsf{T} & \lambda_{m0} & \boldsymbol{\lambda}_{rf}^\mathsf{T} & \boldsymbol{\lambda}_{vf}^\mathsf{T} & m_f & t_f \end{bmatrix}^\mathsf{T},$$

with 15 unknowns. Since τ is prescribed, the residual contains no interior Hamiltonian row:

$$\boldsymbol{R}_\mathrm{fb}^{(3)} = \begin{bmatrix} \boldsymbol{r}^-(\tau) - \boldsymbol{r}_i \\ \boldsymbol{r}^+(\tau) - \boldsymbol{r}_i \\ \boldsymbol{v}^-(\tau) - \boldsymbol{v}^+(\tau) \\ m^-(\tau) - m^+(\tau) \\ \boldsymbol{\lambda}_v^-(\tau) - \boldsymbol{\lambda}_v^+(\tau) \\ \lambda_m^-(\tau) - \lambda_m^+(\tau) \\ \psi_f \end{bmatrix}.$$

The first two residual blocks enforce the fixed interior position from the two propagation directions. The following rows match the variables that remain continuous across the waypoint, and ψ_f enforces the free-final-time condition. Since the event time is prescribed, no interior Hamiltonian row is needed; the position-costate jump is still obtained from $\boldsymbol{\lambda}_r^-(\tau) - \boldsymbol{\lambda}_r^+(\tau)$. Figure 3 shows the landing trajectory, its projections, and the thrust and position-costate histories.

VI. Case D: Collision-Avoidance and Return

The fourth case applies the same event treatment to a low-thrust collision-avoidance maneuver (CAM) followed by a fixed-phase return to the no-maneuver reference orbit. Unlike the previous examples, the interior event is a scalar safety equality rather than a position waypoint or a velocity map. This case tests whether the same forward–backward variable placement is useful in a two-arc design problem where the event also affects the final mission cost.

A. Dynamics and Safety Equality

Only the scalar safety condition needed by the shooting benchmark is retained in the conjunction model. High-order probability-of-collision analysis, B-plane encounter modeling, and practical low-thrust or multiple-impulse CAM design are outside the scope of this example and are treated in detail in the collision-avoidance literature [16, 17, 18].

The fixed-acceleration model uses

$$\boldsymbol{y} = \begin{bmatrix} \boldsymbol{r}^\mathsf{T} & \boldsymbol{v}^\mathsf{T} & \boldsymbol{\lambda}_r^\mathsf{T} & \boldsymbol{\lambda}_v^\mathsf{T} \end{bmatrix}^\mathsf{T},$$

with nondimensional two-body dynamics

$$\dot{\boldsymbol{r}} = \boldsymbol{v}, \qquad \dot{\boldsymbol{v}} = -\frac{\boldsymbol{r}}{r^3} - a_\mathrm{max}\rho\frac{\boldsymbol{\lambda}_v}{\|\boldsymbol{\lambda}_v\|},$$

$$\dot{\boldsymbol{\lambda}}_r = -3\frac{(\boldsymbol{\lambda}_v^\mathsf{T}\boldsymbol{r})\boldsymbol{r}}{r^5} + \frac{\boldsymbol{\lambda}_v}{r^3}, \quad \dot{\boldsymbol{\lambda}}_v = -\boldsymbol{\lambda}_r.$$

The smoothed fuel-optimal throttle is

$$\rho^\star = \frac{2\varepsilon}{\lambda_\mathrm{th} - \|\boldsymbol{\lambda}_v\| + \sqrt{(\lambda_\mathrm{th} - \|\boldsymbol{\lambda}_v\|)^2 + 4\varepsilon^2} + 2\varepsilon}.$$

The CAM condition and corresponding costate-jump direction are

$$g_\mathrm{CAM}(\boldsymbol{r}(\tau)) = d_M^2(\boldsymbol{r}(\tau)) - d_{M,\mathrm{target}}^2 = 0, \qquad P_c = 10^{-6},$$
$$\boldsymbol{\lambda}_r^- - \boldsymbol{\lambda}_r^+ = \alpha\,\nabla_{\boldsymbol{r}} g_\mathrm{CAM}, \tag{8}$$

where d_M^2 is the squared Mahalanobis distance in the encounter B-plane. Thus, as in the earlier examples, the jump magnitude is not a natural quantity to sample before the arcs have been propagated. The numerical setup fixes the reference orbit, spacecraft and propulsion parameters, CAM and return times, target $P_c = 10^{-6}$, and homotopy continuation from $\varepsilon = 10^{-2}$ to 10^{-6}.

B. Forward–Backward Residual

The fixed initial and terminal states are known from the no-maneuver circular reference orbit. The forward–backward shooting vector contains only endpoint costates:

$$\boldsymbol{z}_{\mathrm{fb}}^{(4)} = \begin{bmatrix}\boldsymbol{\lambda}_{r0}^{\mathsf{T}} & \boldsymbol{\lambda}_{v0}^{\mathsf{T}} & \boldsymbol{\lambda}_{rf}^{\mathsf{T}} & \boldsymbol{\lambda}_{vf}^{\mathsf{T}}\end{bmatrix}^{\mathsf{T}},$$

with 12 unknowns. Let $\boldsymbol{Q}_{\perp} \in \mathbb{R}^{3\times 2}$ be any orthonormal basis for the plane normal to $\nabla_{\boldsymbol{r}} g_{\mathrm{CAM}}$. The residual is

$$\boldsymbol{R}_{\mathrm{fb}}^{(4)} = \begin{bmatrix} \boldsymbol{r}^-(\tau) - \boldsymbol{r}^+(\tau) \\ \boldsymbol{v}^-(\tau) - \boldsymbol{v}^+(\tau) \\ \boldsymbol{\lambda}_v^-(\tau) - \boldsymbol{\lambda}_v^+(\tau) \\ g_{\mathrm{CAM}}(\boldsymbol{r}^-(\tau)) \\ \boldsymbol{Q}_{\perp}^{\mathsf{T}}\left(\boldsymbol{\lambda}_r^-(\tau) - \boldsymbol{\lambda}_r^+(\tau)\right) \end{bmatrix}.$$

The first two blocks match the CAM state from the two arcs, and the third block keeps the nonjumping velocity costate continuous. The scalar safety equality sets the event location on the target Mahalanobis-distance surface. The final two rows enforce the direction condition in Eq. (8) by removing any component of the position-costate jump orthogonal to $\nabla_{\boldsymbol{r}} g_{\mathrm{CAM}}$. Since both τ and t_f are fixed, there is no interior Hamiltonian or terminal-time transversality row.

Figure 4 shows the low-Δv joint solution and the homotopy continuation from $\varepsilon = 10^{-2}$ to 10^{-6}.

C. Joint-Design Effect

The joint solution is not merely a convergence test; it changes the mission design outcome. If the 5 h CAM and 7 h fixed-phase return are designed sequentially, the archived fixed-phase solution requires $\Delta v = 0.05164$ m/s. In the joint formulation, the same terminal phase and the same CAM probability are enforced while the two arcs share the event state and the event multiplier. The best joint design uses 0.02650 m/s, nearly half of the sequential fixed-phase value, as shown in Table 1. Because the fixed-acceleration fuel accounting is proportional to the integrated throttle, the same 48.7% reduction applies to propellant consumption.

Tab. 1: Collision-avoidance-return cost comparison

Design strategy	CAM Δv [m/s]	Return Δv [m/s]	Total Δv [m/s]	Saving
Sequential design	0.012957	0.038680	0.051637	n/a
Joint design	0.013346	0.013149	0.026495	48.7%

VII. Formulation Comparison and Numerical Results

This section compares the three shooting formulations under a same random-initialization policy, focusing on how variable placement near physical interior events affects convergence.

A. Shooting-Variable Placement

Table 2 gives root dimensions for orientation; the discussion below focuses on what the variables represent, since dimension alone does not determine shooting difficulty.

Tab. 2: Shooting dimensions

Case	Interior event	Single	Two-forward	Forward-backward
Case A	Mars gravity assist	13	21	17
Case B	moving asteroid encounter	13	19	16
Case C	fixed point	11	19	15
Case D	collision-avoidance and return	9	18	12

The important distinction is the meaning of the unknowns. Single shooting often has the smallest vector, but exposes event-local multipliers, costate jumps, or post-event costates that are not specified by endpoint boundary conditions. Two-forward shooting avoids backward propagation but still guesses event-side augmented states. Forward–backward shooting uses boundary quantities instead and recovers the event jump from the propagated one-sided arcs.

In Case A, the flyby stationarity equations need post-Mars costate information. Single and two-forward shooting expose this downstream information through event-side unknowns, whereas forward–backward shooting obtains it from Vesta-side terminal variables.

In Case B, the difficult local coordinate is the Yandi position-costate jump. Single and two-forward shooting expose that jump or post-encounter event-side states, whereas forward–backward shooting uses Hoth-side terminal quantities with $\boldsymbol{\lambda}_{vf} = \boldsymbol{0}$.

In Case C, the fixed event time removes the Hamiltonian row but not the waypoint position-costate jump. Single and two-forward shooting still expose the jump or post-event augmented state, whereas forward–backward shooting recovers the jump after propagation.

In Case D, the CAM position-costate jump must be parallel to the local safety-gradient direction. Single and two-forward shooting expose this jump or the event-side quantities that generate it, whereas forward–backward shooting uses terminal-boundary unknowns with direct transversality meaning.

B. Random-Initialization Policy

All scripts solve the root system with `MINPACK`, `heyoka` Taylor integration, analytic state-transition sensitivities, and `PyKEP` Lambert or ephemeris calls in the heliocentric cases. The archived `solve_trial` rows count a trial as successful when the maximum residual falls below the case tolerance after root solving, so the rates measure convergence from the stated policy rather than global optimality or continuation performance.

Initial guesses are reference-solution-free; quantities are matched only when their coordinates share physical meaning. Cases A, C, and D use 1000 trials per method, and Case B uses ten 1000-trial seeds per method. The policy uses physical bounds, ephemeris windows, the Case B Lambert terminal-velocity seed for forward–backward shooting, the integrated first-arc continuity seed for two-forward shooting, and the same $[-1, 1]$ landing box for costate, and interior-velocity guesses; no trial perturbs plotted references.

For paired quantities, Case B draws the final time, encounter time, flyby-radius ratio, flyby-plane angle, and costate or jump samples once and maps them to each shooting vector. Case D pairs the single and two-forward guesses, while the forward–backward formulation samples terminal costates directly.

C. Random-Shooting Results

Tab. 3: Random-shooting results.

Case	Single	Two-forward	Forward-backward
A	6/1000 (0.60%)	34/1000 (3.40%)	51/1000 (5.10%)
B	420/10000 (4.20%)	317/10000 (3.17%)	768/10000 (7.68%)
C	72/1000 (7.20%)	236/1000 (23.60%)	241/1000 (24.10%)
D	10/1000 (1.00%)	51/1000 (5.10%)	163/1000 (16.30%)

Table 3 reports empirical success proportions from the listed trials. Under the random-initialization policy used here, the forward–backward advantage in Cases A, B, and D follows the event structure: downstream costates, a moving-target position-costate jump, or a CAM jump aligned with the safety gradient. Case C is nearly tied but still outperformed because the fixed event time and short arcs make the two multi-arc layouts similar, while both avoid the explicit event multiplier used by single shooting.

Case D also has design significance: the joint fixed-phase solution nearly halves the total Δv relative to the sequential design (Table 1).

VIII. Discussion

The experiments show that shooting difficulty depends on sampled coordinates, not only dimension. Single shooting exposes event-local multipliers, jumps, or post-event costates with no endpoint-set scale.

The formulation does not hide the costate discontinuity: the jump still enters the event residual and, for free event times, the Hamiltonian row. The change is coordinate-level: the jump is evaluated after propagation rather than guessed beforehand, so gravity assists, encounters, and waypoints are enforced by event optimality instead of artificial patch-point continuity.

The random initialization is intended to isolate the effect of the shooting formulation rather than represent a complete mission-design strategy. Continuation or shape-based initialization, and global search heuristics remain responsible for trajectory geometry and timing, whereas the proposed residual improves the conditioning of the subsequent local solve near interior events.

Case D also shows design coupling, not only convergence. The joint formulation lets the CAM event satisfy the safety equality while remaining compatible with the fixed-phase return; the sequential design freezes the CAM endpoint first and pays for the resulting phase and velocity mismatch, explaining the 48.7% cost and propellant reduction.

IX. Conclusions

Indirect methods with interior events are often difficult to solve for a practical reason: the event costate jumps usually have no clear physical scale, making the shooting variables more sensitive to initialization even when the PMP conditions themselves are correct.

The main contribution of this work is therefore a different treatment of interior-event variables. Instead of directly solving for the jump conditions, our approach propagates from both sides of the event and recovers the jumps from the propagated costates. The optimality conditions remain unchanged, but the shooting variables become tied to boundary quantities that are easier to initialize and physically interpretable.

The numerical results suggest that, under the random-initialization policy used in this work, the proposed variable representation can have a larger impact on convergence behavior than the use of multiple shooting alone. Across the gravity-assist, flyby, waypoint, and collision-avoidance examples considered here, the proposed approach achieved higher local-convergence success rates than traditional single-shooting and multi-forward-shooting. These results indicate that, for indirect optimization with interior events, local convergence behavior depends on how the shooting unknowns are parameterized. Using a forward–backward shooting in place of event-local costate jumps therefore provides a more numerically stable formulation while preserving the full PMP structure, offering an alternative way to handle interior event constraints in indirect methods.

Acknowledgments

This work was supported in part by the European Union's Horizon Europe Program for Marie Skłodowska-Curie Actions under Grant 101263692.

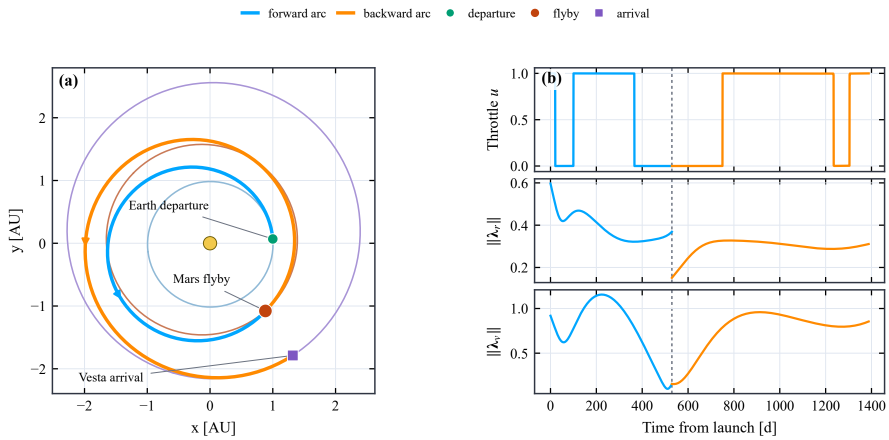

Fig. 1: Dawn gravity assist reference solution. (a) Heliocentric low-thrust arcs and Earth, Mars, and Vesta reference orbits. (b) Smoothed throttle and one-sided position- and velocity-costate norms for $\varepsilon = 10^{-6}$.

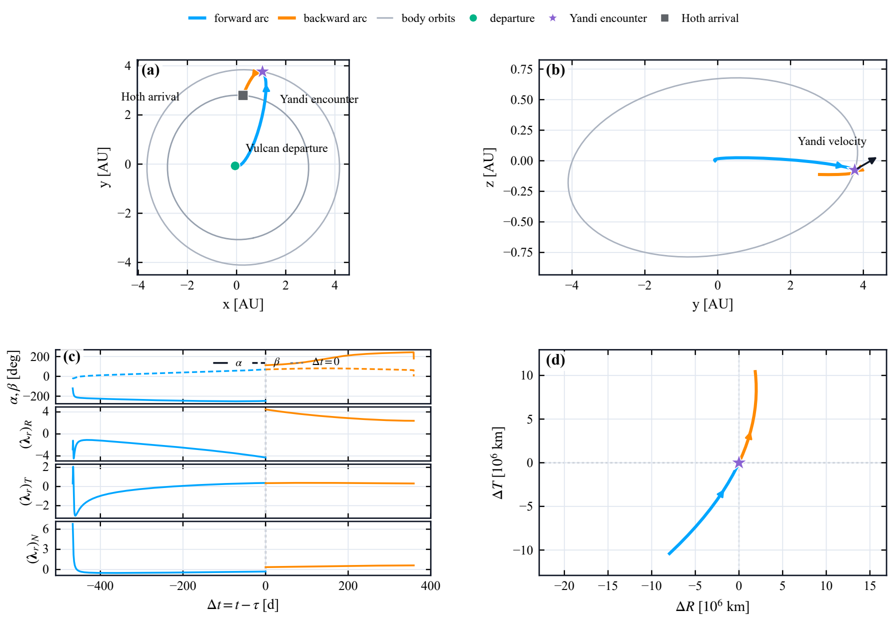

Fig. 2: Solar-sail asteroid encounter. (a) Heliocentric transfer from Vulcan to Hoth through Yandi. (b) Three-dimensional projection near the encounter. (c) Sail control angles and one-sided position-costate components defining the event jump. (d) Yandi-centered trajectory satisfying the moving-point equality on both arcs.

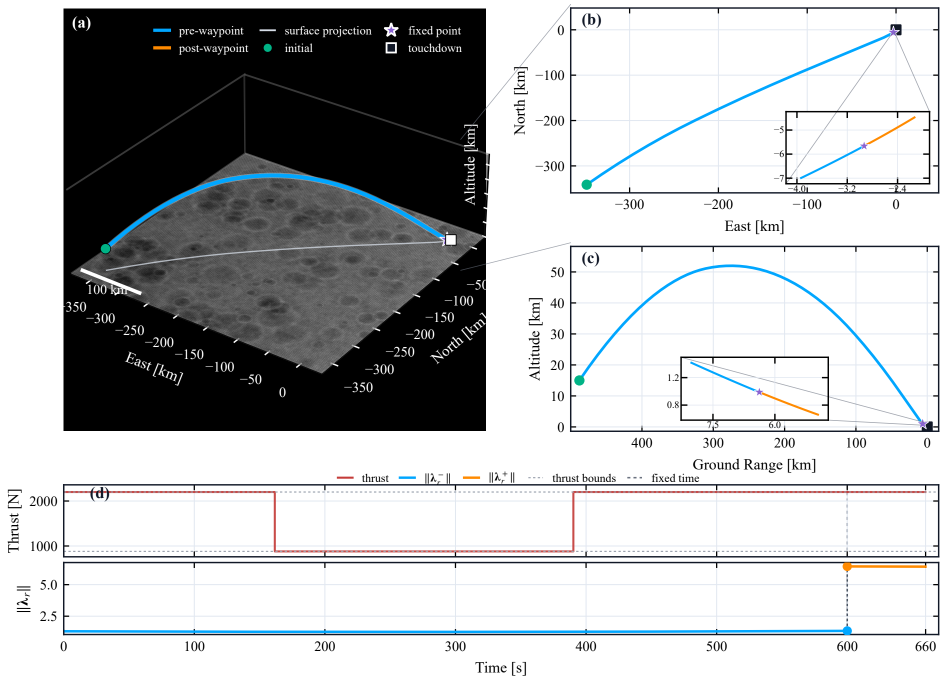

Fig. 3: Lunar landing reference solution. (a) Three-dimensional descent over the lunar-surface plane. (b,c) Horizontal and vertical projections with event-centered inset views. (d) Thrust history and one-sided $\|\boldsymbol{\lambda}_r\|$ histories at the fixed interior time.

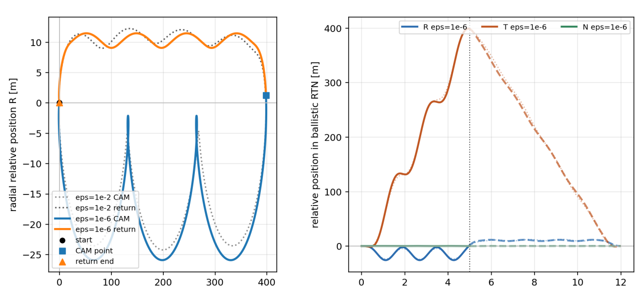

(a) RTN relative trajectory.

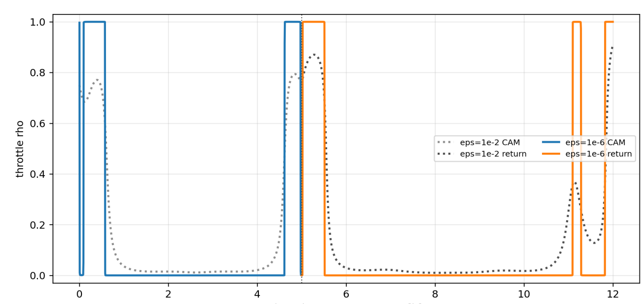

(b) Throttle histories.

Fig. 4: Collision-avoidance-and-return joint solution. (a) CAM and return arcs. (b) Throttle histories.

References

[1] Lev, D., Myers, R. M., Lemmer, K. M., Kolbeck, J., Koizumi, H., and Polzin, K. "The Technological and Commercial Expansion of Electric Propulsion." Acta Astronautica, Vol. 159, pp. 213–227, 2019.

[2] Rayman, M. D., Varghese, P., Lehman, D. H., and Livesay, L. L. "Results from the Deep Space 1 technology validation mission." Acta Astronautica, Vol. 47, No. 2-9, pp. 475–487, 2000.

[3] Russell, C. T. and Raymond, C. A. "The Dawn Mission to Vesta and Ceres." Space Science Reviews, Vol. 163, No. 1, pp. 3–23, 2011.

[4] Betts, J. T. "Survey of numerical methods for trajectory optimization." Journal of guidance, control, and dynamics, Vol. 21, No. 2, pp. 193–207, 1998.

[5] Izzo, D. and Öztürk, E. "Real-Time Guidance for Low-Thrust Transfers Using Deep Neural Networks." Journal of Guidance, Control, and Dynamics, Vol. 44, No. 2, pp. 315–327, 2021. ISSN 0731-5090. doi:10.2514/1.G005254.

[6] Izzo, D. and Origer, S. "Neural representation of a time optimal, constant acceleration rendezvous." Acta Astronautica, Vol. 204, pp. 510–517, Mar. 2023. ISSN 0094-5765. doi:10.1016/j.actaastro.2022.08.045.

[7] D'Ambrosio, A., Benedikter, B., and Furfaro, R. "Physics-Informed Pontryagin Neural Networks for Path-Constrained Optimal Control Problems." Journal of Guidance, Control, and Dynamics, Vol. 48, No. 8, pp. 1861–1877, Aug. 2025. ISSN 0731-5090. doi:10.2514/1.G008854.

[8] Fu, S., Xu, Z., Wu, D., and Gong, S. "Deep Neural Network-Based High-Precision Identification of Weak Stability Boundary Structures." IEEE Transactions on Aerospace and Electronic Systems, Vol. 62, pp. 7208–7223, 2026. doi:10.1109/TAES.2026.3668754.

[9] Vasile, M. and De Pascale, P. "Preliminary Design of Multiple Gravity-Assist Trajectories." Journal of Spacecraft and Rockets, Vol. 43, No. 4, pp. 794–805, 2006. doi:10.2514/1.17413.

[10] Strange, N. J. and Longuski, J. M. "Graphical Method for Gravity-Assist Trajectory Design." Journal of Spacecraft and Rockets, Vol. 39, No. 1, pp. 9–16, 2002. doi:10.2514/2.3800.

[11] Fu, S., Liu, X., Wu, D., Shi, P., and Gong, S. "Energy Transition Domain and Its Application in Constructing Gravity-Assist Escape Trajectories." Journal of Guidance, Control, and Dynamics, Vol. 49, No. 5, pp. 1514–1522, 2026. doi:10.2514/1.G009571.

[12] Zhang, Z., Guo, X., Wu, D., Baoyin, H., Li, J., and Topputo, F. "Global Optimality in Multi-Flyby Asteroid Trajectory Optimization: Theory and Application Techniques." Journal of Guidance, Control, and Dynamics, Vol. 49, No. 5, pp. 1429–1444, May 2026. ISSN 0731-5090, 1533-3884. doi:10.2514/1.G009335.

[13] Zhang, Z., Zhang, N., Guo, X., Wu, D., Xie, X., Li, J., Yang, J., Chen, S., Jiang, F., Baoyin, H., Li, H., Zheng, H., and Duan, X. "GTOC 11: Results from Tsinghua University and Shanghai Institute of Satellite Engineering." Acta Astronautica, Vol. 202, pp. 819–828, Jan. 2023. ISSN 00945765. doi:10.1016/j.actaastro.2022.06.028.

[14] Acikmese, B. and Ploen, S. R. "Convex Programming Approach to Powered Descent Guidance for Mars Landing." Journal of Guidance, Control, and Dynamics, Vol. 30, No. 5, pp. 1353–1366, 2007. doi:10.2514/1.27553.

[15] Pan, B., Ni, Y., Ma, Y., and Lu, P. "Smoothing Homotopy Methods for Solving Nonlinear Optimal Control Problems." Journal of Guidance, Control, and Dynamics, Vol. 46, No. 8, pp. 1470–1484, Aug. 2023. ISSN 0731-5090. doi:10.2514/1.G006977.

[16] Morselli, A., Armellin, R., Di Lizia, P., and Bernelli Zazzera, F. "A High Order Method for Orbital Conjunctions Analysis: Monte Carlo Collision Probability Computation." Advances in Space Research, Vol. 55, No. 1, pp. 311–333, 2015. doi:10.1016/j.asr.2014.09.003.

[17] De Vittori, A., Palermo, M. F., Di Lizia, P., and Armellin, R. "Low-Thrust Collision Avoidance Maneuver Optimization." Journal of Guidance, Control, and Dynamics, Vol. 45, No. 10, pp. 1815–1829, 2022. doi:10.2514/1.G006630.

[18] Armellin, R. "Collision Avoidance Maneuver Optimization with a Multiple-Impulse Convex Formulation." Acta Astronautica, Vol. 186, pp. 347–362, 2021. doi:10.1016/j.actaastro.2021.05.046.

[19] Jiang, F., Baoyin, H., and Li, J. "Practical Techniques for Low-Thrust Trajectory Optimization with Homotopic Approach." Journal of Guidance,

Control, and Dynamics, Vol. 35, No. 1, pp. 245–258, 2012. doi:10.2514/1.52476.

[20] Pontryagin, L. S., Boltyanskii, V. G., Gamkrelidze, R. V., and Mishchenko, E. F. The Mathematical Theory of Optimal Processes. Interscience, 1962.

[21] Sussmann, H. J. “A Maximum Principle for Hybrid Optimal Control Problems.” “Proceedings of the 38th IEEE Conference on Decision and Control,” Vol. 1, pp. 425–430. Phoenix, AZ, USA, 1999.

[22] Guo, T., Li, J., Baoyin, H., and Jiang, F. “Pseudospectral Methods for Trajectory Optimization with Interior Point Constraints: Verification and Applications.” IEEE Transactions on Aerospace and Electronic Systems, Vol. 49, No. 3, pp. 2005–2017, 2013. doi:10.1109/TAES.2013.6558034.

[23] Cerf, M. “Fast Solution of Minimum-Time Low-Thrust Transfer with Eclipses.” Proceedings of the Institution of Mechanical Engineers, Part G: Journal of Aerospace Engineering, Vol. 233, No. 7, pp. 2699–2714, 2019. doi:10.1177/0954410018785971.

[24] Zhang, C., Topputo, F., Bernelli-Zazzera, F., and Zhao, Y.-S. “Low-Thrust Minimum-Fuel Optimization in the Circular Restricted Three-Body Problem.” Journal of Guidance, Control, and Dynamics, Vol. 38, No. 8, pp. 1501–1510, Aug. 2015. ISSN 0731-5090. doi:10.2514/1.G001080.

[25] Gao, Y. and Kluever, C. “Low-Thrust Interplanetary Orbit Transfers Using Hybrid Trajectory Optimization Method with Multiple Shooting.” “AIAA/AAS Astrodynamics Specialist Conference and Exhibit,” Guidance, Navigation, and Control and Co-located Conferences. American Institute of Aeronautics and Astronautics, Aug. 2004. doi:10.2514/6.2004-5088.

[26] Sidhoum, Y. and Oguri, K. “Indirect Forward–Backward Shooting for Low-Thrust Trajectory Optimization in Complex Dynamics.” Journal of Guidance, Control, and Dynamics, Vol. 47, No. 10, pp. 2164–2172, 2024. ISSN 0731-5090. doi: 10.2514/1.G007997.

[27] Englander, J. A. and Conway, B. A. “Automated Solution of the Low-Thrust Interplanetary Trajectory Problem.” Journal of Guidance, Control, and Dynamics, Vol. 40, No. 1, pp. 15–27, Jan. 2017. ISSN 0731-5090. doi:10.2514/1.G002124.

[28] Sims, J. A. and Flanagan, S. N. “Preliminary Design of Low-Thrust Interplanetary Missions.” “AAS/AIAA Astrodynamics Specialist Conference,” 1999. AAS 99-338.

[29] Rayman, M. D., Fraschetti, T. C., Raymond, C. A., and Russell, C. T. “Dawn: A Mission in Development for Exploration of Main Belt Asteroids Vesta and Ceres.” Acta Astronautica, Vol. 58, No. 11, pp. 605–616, 2006. doi:10.1016/j.actaastro.2006.01.014.

[30] Giorgini, J. D., Yeomans, D. K., Chamberlin, A. B., Chodas, P. W., Jacobson, R. A., Keesey, M. S., Lieske, J. H., Ostro, S. J., Standish, E. M., and Wimberly, R. N. “JPL’s On-Line Solar System Data Service.” Bulletin of the American Astronomical Society, Vol. 28, p. 1158, 1996.

[31] Bertrand, R. and Epenoy, R. “New smoothing techniques for solving bang–bang optimal control problems—numerical results and statistical interpretation.” Optimal Control Applications and Methods, Vol. 23, No. 4, pp. 171–197, 2002. ISSN 1099-1514. doi:10.1002/oca.709.

[32] Jet Propulsion Laboratory. “GTOC13: The Problem.”, 2025. Accessed 1 May 2026.